Deeply Virtual Electroproduction of Vector Mesons

J.-P. Didelez, M.-A. Duval, <u>M. Guidal</u>[†‡§], E. Hourany
Institut de Physique Nucléaire, F-91406 Orsay, France

M. Vanderhaeghen
Institut für Kernphysik, University Mainz, D-55099 Mainz, Germany

V. Burkert, F. Klein, K. Loukachine, <u>E. Smith</u>[†]
Jefferson Lab., Newport-News, VA, USA

G. Audit, P.A.M. Guichon, N. d'Hose, J.M. Laget, <u>C. Marchand</u>[†] ,
J. Marroncle, P. Vernin
Service de Physique Nucléaire, C.E.A Saclay, F-91191 Gif-sur-Yvette, France

C. Djalali, B. Preedom, D. Tedeschi, S. Whisnant
Univ. South Carolina, SC, USA

J.P. Boquet, A. Lleres, C. Perrin, D. Rebreyend
ISN, Grenoble, France

P.L. Cole
Univ. of Texas at El Paso, TX, USA

L. Elouadrhiri
Christopher Newport University & Jefferson Lab., Newport-News, VA, USA

S. Dytman, J. Mueller
Univ. of Pittsburgh, PA, USA

C. Hyde-Wright
Univ. of Old Dominion, Norfolk, VA, USA

M. Anghinolfi, M. Battaglieri, P. Corvisiero, M. Ripani, G. Ricco, M. Sanzone,
M. Taiuti
INFN, Genova, Italy

<u>+ the CLAS collaboration</u>

[†]spokesperson

[‡]will present the proposal

[§]contact person

1

I. INTRODUCTION

We propose to measure with the CEBAF Large Acceptance Spectrometer (CLAS) the exclusive electroproduction of the vector mesons ρ, ω and ϕ on the nucleon in the Bjorken regime ($Q^2, \nu \gg$ and $x_B = \frac{Q^2}{2M\nu}$ finite). The study of the x_B and t dependence of these reactions in the Bjorken regime holds promise, through perturbative QCD, to access new structure functions of the nucleon, the so called "Off-Forward Parton Distributions" (OF-PD's) [1] [2] [3] [5]. These structure functions are a generalization of the parton distributions measured in the deep inelastic scattering experiments and their first moment links them to the elastic form factors of the nucleon. Furthermore, Ji [1] has shown that their second moment gives access to the sum of the quark spin and the quark orbital angular momentum to the nucleon spin, which may shed a new light on the "spin-puzzle". It is clear that the actual determination of the OFPD's will require a more extended and ambitious experimental program. Our goal is to make a first step in this direction. Namely, we propose to test experimentally the Q^2 scaling law predicted by pQCD in the Bjorken regime. This is a prerequisite to the development of this field.

The combination of the Jefferson Lab (JLab) 6 GeV continuous electron beam and of the large acceptance CLAS detector will allow to reach values in Q^2 up to $\approx 4.$ GeV^2 with reasonnable count rates. More precisely, from an experimental point of view, one has to identify the reaction channels $\gamma_L^* p \rightarrow p(\rho_L^0, \omega_L, \phi_L)$ where the index L stands for the *longitudinal* polarization state of the particles. For these channels, perturbative QCD (PQCD) at leading order predicts that the longitudinal differential cross-section $\frac{d\sigma_L}{dt}$ follows a $\frac{1}{Q^6}$ dependence [3].

The experimental program that we propose consists in several points :

- Measure the Q^2 dependence of the reactions $\gamma_L^* p \rightarrow p(\rho_L^0, ...)$ up to $Q^2 \approx 4$ GeV^2. This

will allow to study the transition from meson exchange mechanisms at low Q^2 to quark exchange processes at larger Q^2. At higher values of Q^2, one will test the onset of the $\frac{1}{Q^6}$ <u>scaling</u> behavior of the cross section predicted by PQCD.

- The longitudinal vector mesons (ρ_L^0, ...) will be identified through the vector meson decay angular distribution. Assuming SCHC (s-channel helicity conservation) [4] permits to extract the cross section for the reaction $\gamma_L^* p \rightarrow p(\rho_L^0, \omega_L, \phi_L)$. We will check the validity of the SCHC hypothesis by studying those vector meson decay density matrix elements that are zero when SCHC applies.

- If we indeed reach the Bjorken regime where scaling shows up, an analysis of the x_B and t dependence of the cross sections may allow a first exploratory analysis of the OFPD's.

This experiment is the first one to explore this new domain of hadronic physics : the OFPD's. This subject is currently in full expansion on the theoretical side. Other experimental facilities, such as COMPASS and HERMES, are currently considering a similar study of the OFPD's. In spite of the relatively "low" energy of the incident beam, the high luminosity and the better resolution that one can reach with CLAS will allow equivalent count rates to the two other facilities in the same kinematical range (but in a closer and shorter period). The perspective of a rich experimental program opens up for the coming decade.

Exclusive photo- and electroproduction of vector mesons is also receiving a renewed interest in other kinematical regimes investigated in two other JLab experiments that are currently taking data. Firstly, Exp. 93-031 [7] studies of the photoproduction of vector mesons (with a special emphasis on the ϕ) at large t to see possible manisfestations of hard scattering mechanisms compared to the traditional diffractive Pomeron exchange mechanism in photoproduction at low t. Another experiment (Exp. 93-022 [8]) addresses the issue of a possible strange component in the ground state of the nucleon, via the electroproduction of ϕ meson at moderate momentum transfers (Q^2 values up to 2 GeV^2).

In the present experiment, we propose to investigate the electroproduction of vector mesons at moderate energies (W in the range 2 - 3 GeV) but high virtuality Q^2 (Q^2 up to 4 GeV^2) of the photon to study the link between these electroproduction cross sections and the OFPD's.

We begin by reviewing in Section II the physics motivation of the OFPD's. In Section III, the status of the existing data will be discussed. The measurement proposed is presented in Section IV and the estimates and simulations are shown that we carried out to show the feasibility of this experiment at Jefferson Lab with the CLAS detector.

II. THE PHYSICS CASE

We now give a brief overview of the physics of the OFPD's. The following calculations and developments for this vector meson electroproduction experiment were mainly performed by M. Vanderhaeghen and are presented in Refs. [5] [6]. The detailed theoretical formalism and the definitions of the kinematical variables are presented in the Appendix.

Recently, Ji [1] and Radyushkin [2] have proposed that Deeply Virtual Compton Scattering (DVCS) in the Bjorken regime ($Q^2, \nu \gg$ and $x_B = \frac{Q^2}{2M\nu}$ finite) could be used to access a new type of parton distributions, generally referred to as "Off-Forward Parton Distributions" (OFPD's). They have shown that the leading order DVCS amplitude in forward direction can be factorized in a hard scattering part (exactly calculable in PQCD) and a nonperturbative nucleon structure part as is illustrated in Fig.(1).
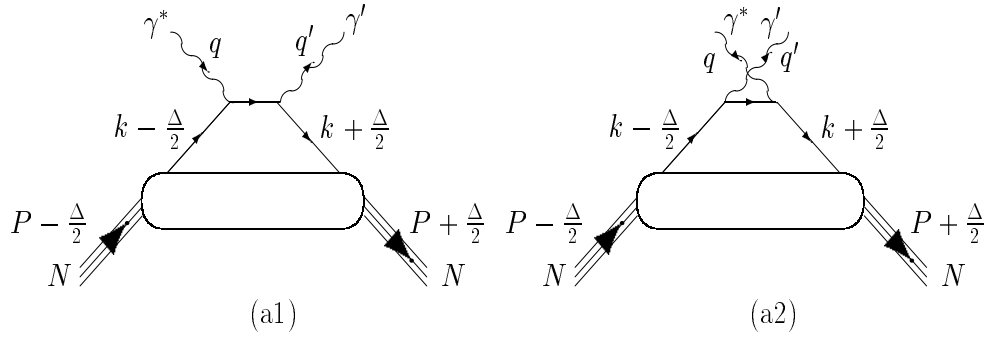
4

FIG. 1. Handbag diagrams for DVCS.

In these so-called "handbag" diagrams of Fig.(1), the lower blob which represents the structure of the nucleon can be parametrized, at leading order PQCD in $\frac{1}{Q^2}$, in terms of 4 generalized structure functions, called the Off-forward parton distributions (OFPD's). These are defined as $H, \tilde{H}, E, \tilde{E}$, and depend upon three kinematical invariants : x, ξ, t (see Appendix). H and E are spin independent and $\tilde{H}$ and $\tilde{E}$ are spin dependent. The OFPD's H and $\tilde{H}$ are actually a generalization of the parton distributions measured in deep inelastic scattering. Indeed, in the forward direction (defined by $q = q'$), H reduces to the quark distribution and $\tilde{H}$ to the quark helicity distribution measured in deep inelastic scattering. Furthermore, at finite momentum transfer, there are model independent sum rules which relate the first moments of these OFPD's to the elastic form factors (see Appendix).

The OFPD's reflect the structure of the nucleon independently of the reaction which probes the nucleon. They could also be accessed through the hard exclusive electroproduction of mesons (π^0, ρ^0, ω, ϕ,...) for which a QCD factorization proof was given recently [3]. These processes are illustrated on Fig.(2). According to Ref. [3], the factorization applies when the virtual photon is longitudinally polarized because in this case, the end-point contributions in the meson wave function are power suppressed. It was also shown in Ref. [3] that the cross section for a transversly polarized photon is suppressed by $1/Q^2$ compared to a longitudinally polarized photon. Because the transition at the upper vertices of Fig.(2) will be dominantly helicity conserving at high energy and in the forward direction, this

means that the vector meson will also be predominantly longitudinally polarized (notation $\rho_L^0, \omega_L, \phi_L$) for a longitudinal photon. By identifying then the polarization of the vector meson through its decay angular distribution, one can obtain the longitudinal part.

FIG. 2. (a) Diagram for the factorized meson electroproduction amplitude. (c) Leading order diagrams for the hard scattering part T_H of the meson electroproduction amplitude.

Experimental tests of the s-channel helicity conservation are possible by measuring the vector meson decay density matrix elements, as most of them vanish when SCHC holds. This was e.g. done at lower Q^2 in Ref. [18].

It has been shown in [3] that leading order PQCD predicts that the vector meson channels $(\rho_L^0, \omega_L, \phi_L)$ are sensitive only to the unpolarized OFPD's (H and E) whereas the pseudo-scalar channels $(\pi^0, \eta, ...)$ are sensitive only to the polarized OFPD's ($\tilde{H}$ and $\tilde{E}$). For the electroproduction of pseudoscalar and vector mesons the leading order amplitude at large x_B (i.e. in the valence region) is given by the diagrams of Fig.(2) and was calculated in Ref. [5] using asymptotic meson distribution amplitudes.

6

In comparison to meson electroproduction, we recall that DVCS depends at the same time on *both* the polarized and unpolarized OFPD's (Eq.(A1)). In any case, it is clear that all these different channels $\gamma^* p \to p(\gamma, \pi^0, \rho^0, \omega, \phi, ...)$ are highly complementary because, apart from isospin factors, they depend on the same OFPD's and provide mutual constraints. This entices to start a whole experimental program to study these different reactions at large Q^2 and their sensitivity to the OFPD's.

These large Q^2 domains in the valence region ($x_B \simeq 0.3$) are mostly unexplored experimentally (data are very scarce and imprecise, see section III for a discussion of existing data) and, for a first exploratory approach, we will now show that the meson channels hold the best promises due to the relatively high cross-sections. First estimates for the π^0, ρ_L^0 cross sections were given in Refs. [5] [6] besides the γ-channel using an educated guess for the OFPD's, which consists of a product of elastic form factors by quark distributions measured in DIS. This ansatz satisfies the first sum rules and the corresponding distributions obviously reduce to the quark distributions from DIS in the forward direction.

Fig. 3 shows these results for the total ρ_L^0 electroproduction cross section as a function of the C.M. energy W for different values of Q^2.

At high C.M. energies, it is well known that the Perturbative Two Gluon Exchange Mechanism (PTGEM) dominates as soon as $Q^2 \gtrsim 6$ GeV^2 and this mechanism also implies a $\frac{1}{Q^6}$ behavior of σ_L [12] [13] (The PTGEM mechanism is illustrated on Fig.(4)). The PTGEM explains well the fast increase at high energy of the cross section which is also confirmed by the more recent ZEUS data [15]. However, the PTGEM substantially underestimates the data at lower energies (around $W \approx 10$ GeV). And this is the region where the quark exchange mechanism (QEM) of Fig.(2) is expected to contribute ($W \lesssim 10$ GeV corresponds to x_B in the valence region at the high Q^2 values shown). Fig.(3) provides a strong hint that the deviation from the PTGEM of the data at lower energies can be attributed to the onset of the QEM. Furthermore, data from HERMES [17] in the W region 4 - 6 GeV and for Q^2 values up to 4 GeV^2 will be able to provide further evidence for a quark exchange

mechanism. Going down in energy (but staying above the resonance region), the sensitivity to the QEM and consequently to the off-forward quark distributions increases. Fig. 2 shows the region accessible at JLab, i.e. the valence region ($x_B \simeq 0.3$) where the QEM is maximal.
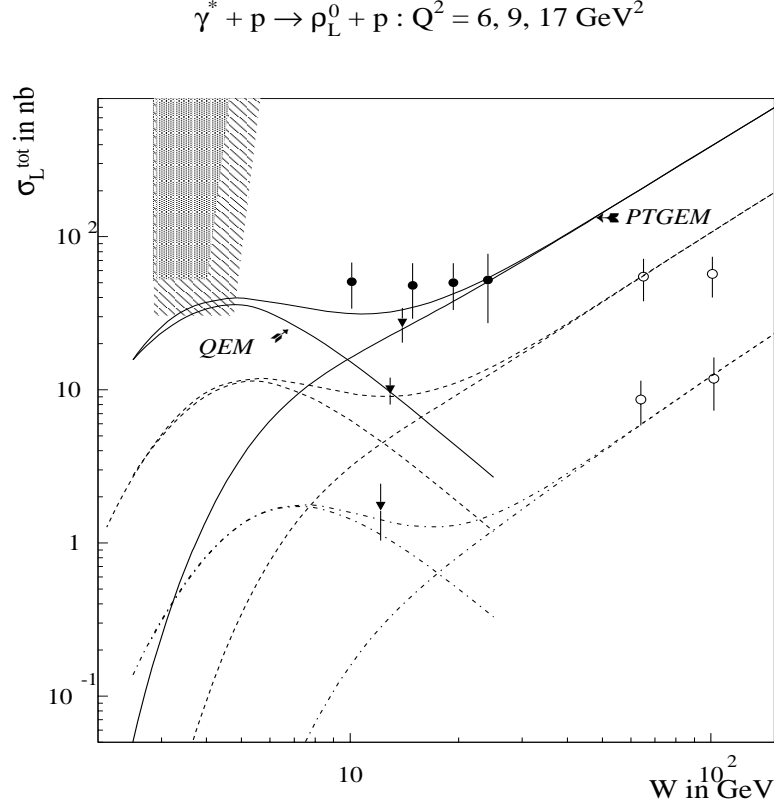
$$\gamma^* + p \rightarrow \rho_L^0 + p : Q^2 = 6, 9, 17 \text{ GeV}^2$$

FIG. 3. Total longitudinal cross section for ρ_L^0 electroproduction as calculated in Ref. [5]. Data from NMC [9] (triangles) at $Q^2 = 5.5$ (highest point), 8.8 and 16.9 (lowest point) GeV^2, E665 [10] (black circles) at $Q^2 = 5.6$ GeV^2 and ZEUS [11] (open circles) at $Q^2 = 8.8$ (upper points) and 16.9 GeV^2 (lower points). Calculations are shown at $Q^2 = 6$ GeV^2 (full lines), $Q^2 = 9$ GeV^2 (dashed lines) and $Q^2 = 17$ GeV^2 (dashed-dotted lines). The curves which grow at high W correspond with gluon exchange whereas the curves which are peaked below W ≈ 10 GeV correspond with quark exchange. The incoherent sum of both mechanisms is also shown. The two shaded areas on the top left part of the plot show the regions kinematically accessible at JLab with a 6 GeV and a 8 GeV electron beam (smaller and larger area respectively).
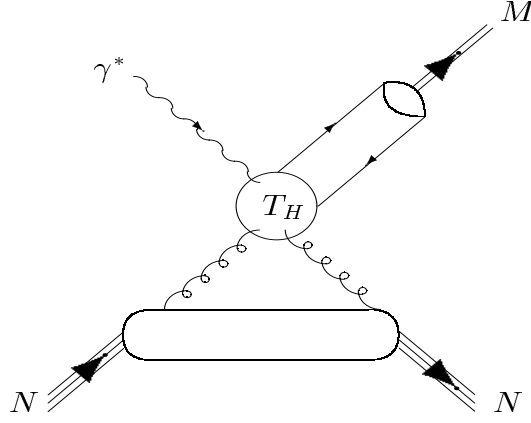
8

FIG. 4. Perturbative 2-gluon exchange mechanism [12] [13].

We compare on Fig.(5) the angular dependence of the 5-fold differential cross section $\frac{d\sigma}{dk^e_{Lab}d\Omega^e_{Lab}d\Omega^M_{Lab}}$ for the 4 channels $\gamma, \pi^0, \rho^0_L, \omega_L$. It is clear on this picture that the ρ channel is very favorable. Its cross section is the highest because it depends on the unpolarized OFPD's (H and E). The ω_L channel has a cross section that is substantially higher than the ratio $\sigma_\omega/\sigma_\rho = \frac{1}{9}$ predicted by the diffractive mechanism and this is essentially due to the QEM. The ω_L and ρ^0_L channels probe different combination of the u and d OFPD's and a measurement of both therefore allows to separate these u and d-quark unpolarized OFPD's. The π^0 channel depends on the polarized OFPD's ($\tilde{H}$ and $\tilde{E}$) and therefore has a lower cross section. The DVCS is proportional to *both* the polarized and the unpolarized OFPD's as was already mentioned but it has an extra α_{em} coupling (due to the final state photon) which reduces the cross section. (By comparison, the meson final states go through the exchange of a gluon and therefore a α_S coupling). Furthermore, at JLab energies, the DVCS suffers from the competing process which leads to the same final state, the Bethe-Heitler process. This extra "parasite" mechanism is dominant at 6 GeV and renders the extraction from the cross section of the DVCS process very difficult. This "parasite" process is absent in the case of meson electroproduction. The ϕ_L channel does not look too promising at 6 GeV but it is seen that its cross section rises sharply at an incident electron energy of 8 GeV (due to the increased flux factor entering the cross section).

9

It should then become accessible experimentally and holds the enthusiasming perspective to probe the strange content of the nucleon and in particular, to extract, in an alternative fashion to parity violation experiments, the strange form factors of the nucleon.
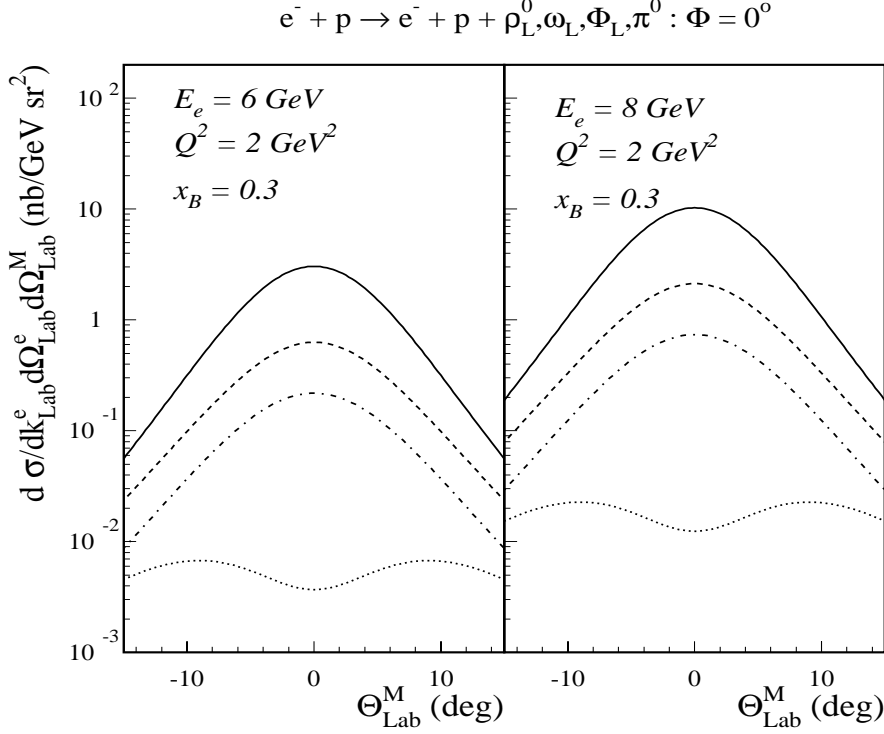
$$e^- + p \rightarrow e^- + p + \rho_L^0, \omega_L, \Phi_L, \pi^0 : \Phi = 0^o$$

FIG. 5. Comparison between the ρ_L^0 (full lines), ω_L (dashed lines), π^0 (dashed-dotted lines) and ϕ_L (dotted lines, only F_1^s contribution shown) channels at JLab at 6 GeV (left panel) and 8 GeV (right panel).

Before considering the extraction of the OFPD's from the data, we mentioned in the introduction that it is mandatory to first demonstrate that the scaling regime has been reached. On Fig.(6), we show the forward $\gamma, \pi^0, \rho_L^0, \omega_L$ cross section as a function of Q^2. In leading order PQCD, the DVCS transverse cross section $\frac{d\sigma_T}{dt}$ behaves as $\frac{1}{Q^4}$. The mesons' longitudinal cross sections are predicted to obey a $\frac{1}{Q^6}$ scaling. The figure also shows the lever arm reachable at JLab : with a maximum "theoretical" Q^2 of ≈ 4 GeV^2, the cross

section can be measured over about a decade. This provides a sufficient lever arm to test the scaling prediction.

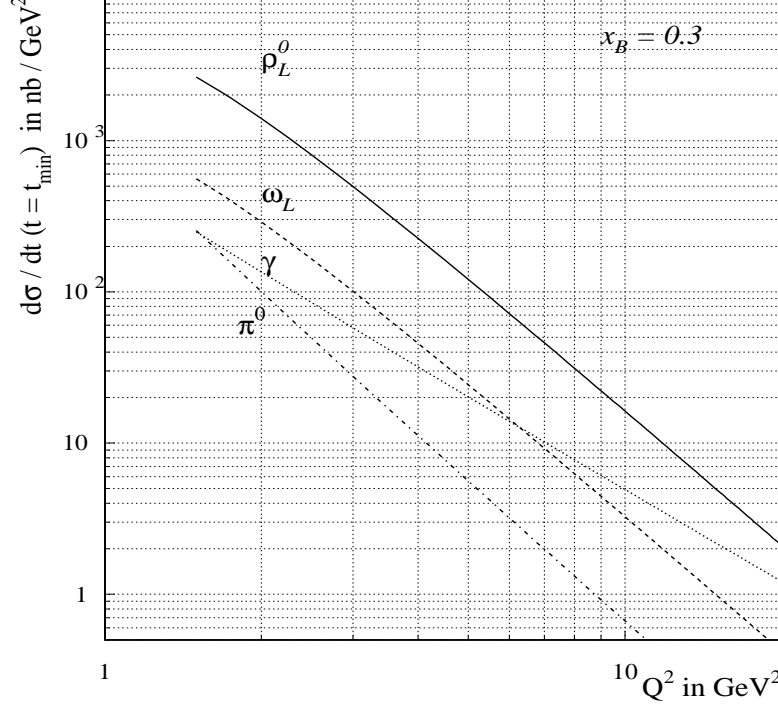$$\gamma^* + p \rightarrow M + p : (M = \rho_L^0, \omega_L, \Phi_L, \pi^0, \gamma)$$

FIG. 6. Scaling behavior of the forward $(t = t_{min})$ differential cross section $\frac{d\sigma_L}{dt}$ for the $\pi^0, \rho_L^0, \omega_L$ channels and $\frac{d\sigma_T}{dt}$ for the γ channel.

III. EXISTING DATA

In Fig.3, we have shown that existing data at intermediate W values (around $W \approx 10$ GeV) may provide a first hint of a quark exchange mechanism at large Q^2. On the low Q^2 side, several data for exclusive electroproduction of vector mesons have been taken [18] [19].

In Ref. [18], DESY data for exclusive ρ^0 electroproduction are shown in the W region 1.3 - 2.8 GeV and in the Q^2 range 0.3 - 1.4 GeV^2. The ρ^0 decay angular distribution has been measured and a test of s-channel helicity conservation (SCHC) was performed. It was

11

found that for $2.1 < W < 2.8$, $0.3 < Q^2 < 1.4$ and for $|t| < 0.5$ GeV^2, the helicity single-flip amplitudes are of the order 15-20 % of the non-flip amplitudes (furthermore, double-flip amplitudes were found to be smaller than single-flip amplitudes). This gives an upper limit of the violation of SCHC that we should encounter in our present experiment (The leading order PQCD formalism leads asymptotically to helicity conserving amplitudes). Assuming SCHC, longitudinal rhos are produced by longitudinal photons only and transverse rhos by transverse photons only. From the ratio of longitudinal to transverse rhos, we further see that the ratio $R = \sigma_L/\sigma_T$ rises linearly with Q^2 up to $Q^2 = 1$ GeV^2.

The existing data which come the closest to the JLab range from the low Q^2 side were obtained at Cornell [19], where the exclusive ρ^0, ω and ϕ electroproduction has been measured in the range $1.9 < W < 4$ GeV (above the resonance region) and $0.7 < Q^2 < 4$ GeV^2.

In this kinematical range, a clear ρ peak has been identified as is shown on Fig.7. It is seen on Fig.7, that for the highest values of Q^2 that were measured at Cornell, the background under the ρ peak diminishes when one goes to higher values of W (which is the region of our concern). The ratio σ_L/σ_T was measured at Cornell by assuming SCHC in agreement with the results of Joos et al. [18] and a value of the order of 1 was found between $1 < Q^2 < 3$ GeV^2.

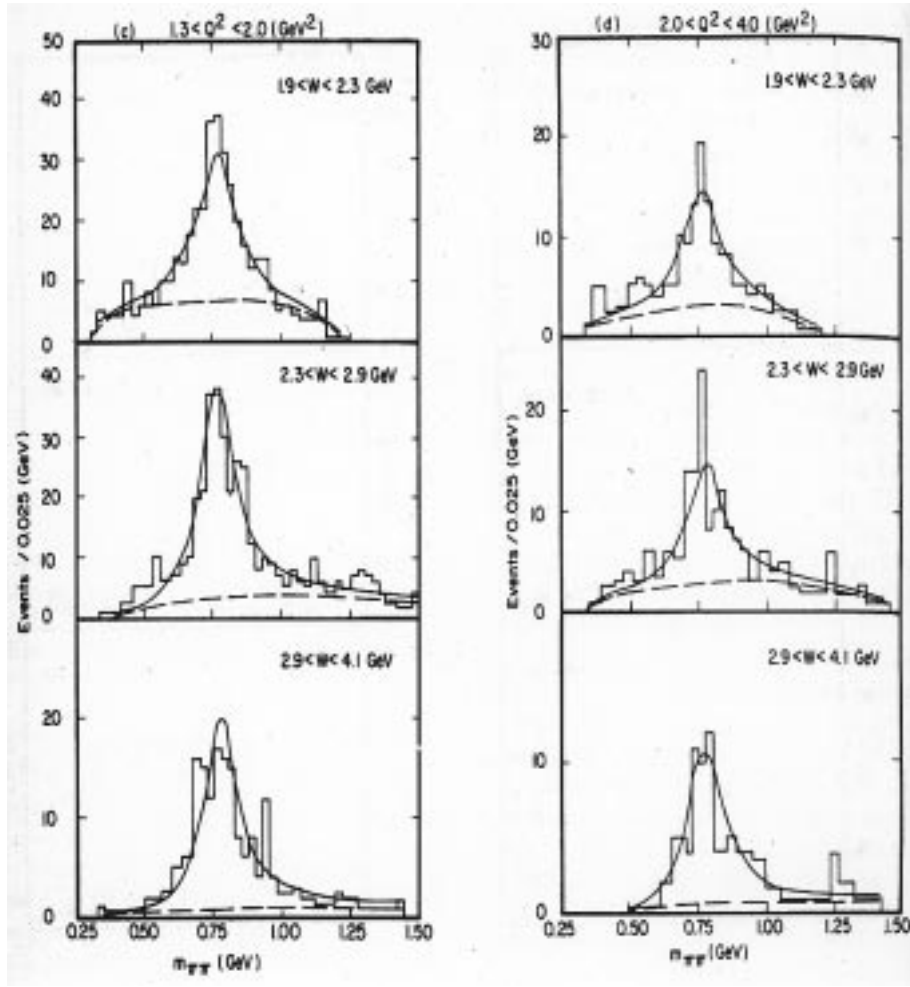FIG. 7. $\pi^+\pi^-$ invariant mass distributions as measured in Cornell [19] in the Q^2 ranges 1.3 - 2.0 GeV^2 (left) and 2.0 - 4.0 GeV^2 (right) as function of the energy W. The solid curves are the fits to the total mass distribution whereas the dashed curves are the sum of the Δ^{++}, Δ^0 and phase-space contributions determined by the fits.

In Fig.8, the longitudinal ρ total cross section (as deduced from an exponential form for the forward differential cross section) is shown as function of Q^2 with the Cornell data. For comparison, the prediction of the QEM in terms of the OFPD's is also shown for the average value of $W = 2.65$ GeV and is extrapolated to the lower Q^2 of the Cornell data. It is seen that the order of magnitude of this QEM prediction which was found on Fig.3 to be compatible with the data at higher Q^2, is also roughly in agreement with the Cornell data

13

at lower Q^2. However, as can be seen from the large Q^2 bins (see also the low statistics of Fig.7), these data do not have the precision and do not have a sufficiently large lever arm in Q^2 to test a Q^2 scaling behaviour of the leading order PQCD amplitude. Furthermore, the data of figure 8 mix different x_B values which prevents any conclusion. It can also be noted on figure 8 the incompatibility of the data at large Q^2 (compare the "square" and "triangle" data points which cross each other at $Q^2 = 1.65$ GeV^2 and $Q^2 = 3.$ GeV^2).

It should be clear that more precise data (also over a larger Q^2 range and at <u>fixed</u> x_B) are needed to realize the study that we propose.

$$\gamma^* + p \rightarrow \rho_L^0 + p$$
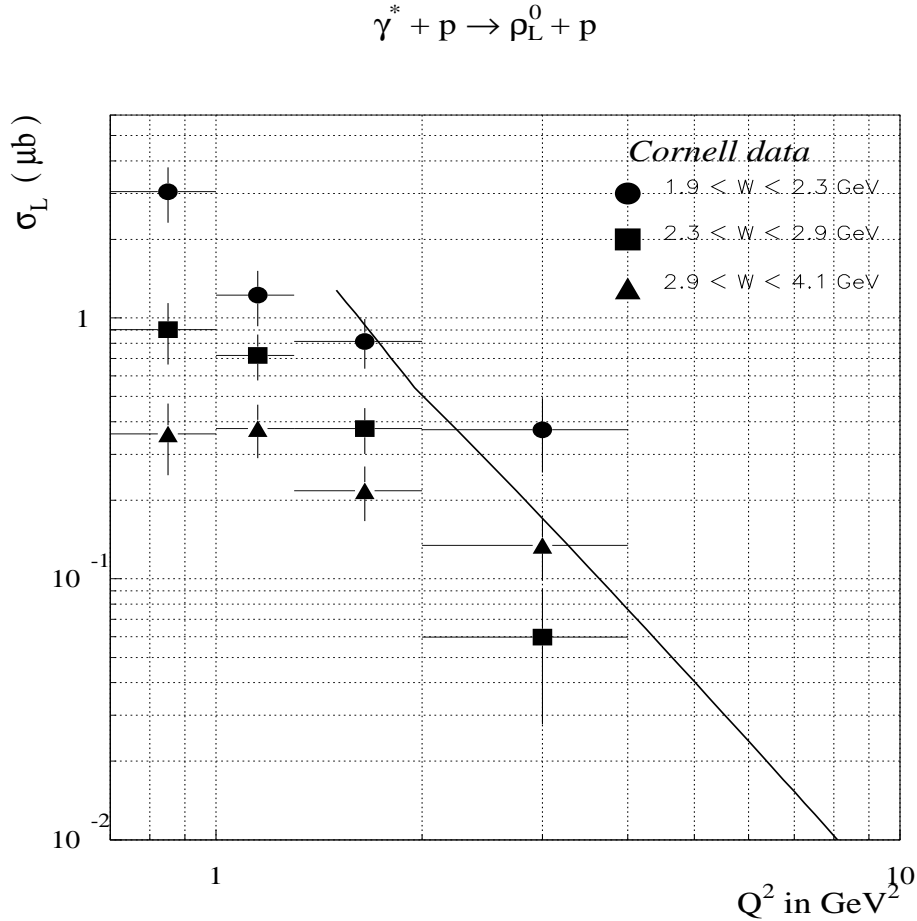
FIG. 8. Longitudinal cross section data for exclusive ρ^0 electroproduction from Cornell [19] for W in the range 2 - 4 GeV and Q^2 values up to 3 GeV^2. The solid curve is the calculation for ρ_L^0 electroproduction using the OFPD's at the average value $W = 2.65$ GeV of the Cornell data.

At Cornell the ω electroproduction has also been measured in the same kinematical range

as for the ρ. As is well known, a diffractive mechanism predicts a 1:9 ratio for $\sigma_\omega/\sigma_\rho$. The ω/ρ ratio for the Cornell data is shown in Fig.9. It is seen that in the range $2.8 < W < 3.7$ GeV, a ratio that is comparable to the one of a diffractive mechanism is found. However at lower W, a substantially higher ratio was found. At the photoproduction point this is understood as being due to the contribution of π^0 exchange to ω photoproduction which dominates at lower W compared to the pomeron exchange mechanism at high W, which gives a ratio of 1:9. Going to higher Q^2, this higher ω/ρ ratio in the region $W = 2$ - 3 GeV might be some further indication of a quark exchange mechanism. It was indeed seen in Fig.5 that the QEM predicts a ω/ρ ratio of about 1:5 in the valence region which is about twice as much as in the diffractive domain. The value of this ratio in the QEM is determined by the u and d-quark OFPD's.
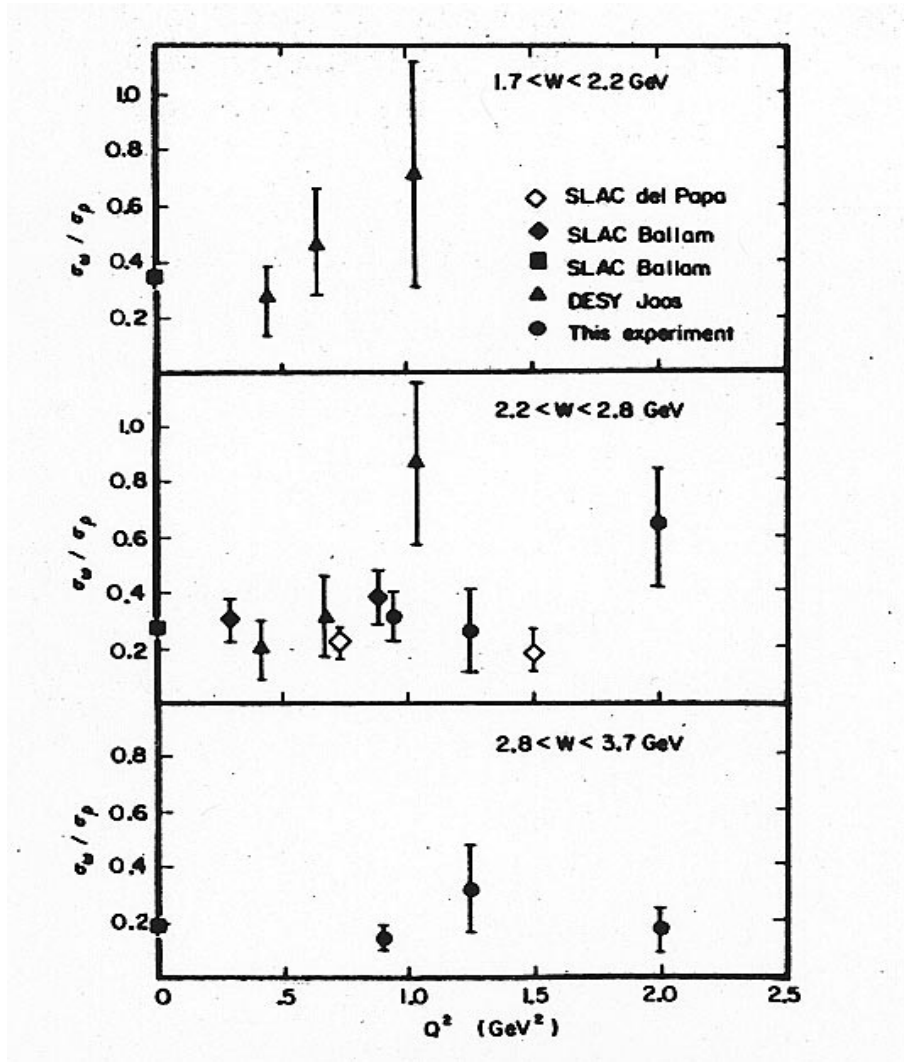
FIG. 9. ω/ρ^0 ratio at different W as function of Q^2. The data are from Cornell [19].

Beyond data already available

In the next section, it will be shown firstly how the proposed measurement on vector meson electroproduction with CLAS at JLab can substantially improve the accuracy in the range covered previously by the Cornell data. Secondly, it will be shown how the kinematical range of these previous data can be extended at JLab to $Q^2 \approx 4$ GeV^2 with $E_e = 6$ GeV.

IV. FEASIBILITY OF THE EXPERIMENT

A. Overview of the experiment

We briefly recall here the main steps of the proposed experiment.

- Measure the Q^2 dependence of the reaction $\gamma_L^* p \to p(\rho_L^0, ...)$.

- Identify the longitudinal vector meson ρ_L^0 can be identified through the vector meson decay angular distribution. Assuming SCHC in a first stage permits us to extract the desired cross section for $\gamma_L^* p \to p(\rho_L^0, ...)$.

- Test of the SCHC hypothesis by considering the inference response functions R_{TT} and R_{TL} which are accessible with a large acceptance detector such as CLAS.

- Measure the x_B and t dependences of the cross section. If we are in the scaling regime, this analysis permits us then to perform a first exploration of the OFPD's.

We will now present the studies we carried out to show to which extent the program we have outlined above will be feasible at JLab with the CLAS detector. The use of a large acceptance detector is needed for two reasons. First, one has to identify longitudinally from transversely polarized vector mesons as was mentioned in the previous section and this can be done by measuring the angular distribution of the decay products of the vector meson, which means, in addition to the electron and the proton, the detection of an extra particle (a pion for the ρ and the ω and a kaon for the ϕ). Second, it is necessary to cover as large a kinematical domain in x, t and Q^2 as possible if one has the perspective to deconvoluate the OFPD's from the differential cross sections. The objective is therefore to "bin" as finely as possible the (x_B, t, Q^2) space.

We first investigate the acceptance issues and the phase space which can be accessed with CLAS. In the following, we will use the FASTMC program [23] to simulate the response (acceptance, resolution) of the CLAS detector. Our event generator of meson electroproduction

- adapted from Ref. [22] - has for input the cross sections of the model presented in the previous section [5]. We generated events with an electron beam energy of 6 GeV assuming a luminosity of 10^{34} cm^{-2}s^{-1} and 400 hours of beam time. We restricted our study to $Q^2 > 1.5$ GeV^2 and $-t < 1.5$ GeV^2, as our domain of interest is the large Q^2 and small t region, as outlined in the previous section, and also to $W > 2$ GeV to stay above the resonance region.

B. Phase space, acceptances and resolutions

1. Acceptances

Figure 10 shows the results of the acceptance studies for the kinematical variables Q^2, x_B, W and t. It shows the kinematical domains which can be accessed in CLAS with a 6 GeV beam : in particular, Q^2 up to ≈ 4. GeV^2 and W up to 3.2 GeV. In these domains, with the requirement based on the detection of the three particles e,p,π^+, the combined acceptance and efficiency are almost all between 15 and 20%. Of course, Q^2, x_B, W (and ν) are all correlated and Fig. 11 shows these correlations. One should in particular notice the two well-known kinematical effects :

- As W increases, the Q^2 domain decreases,

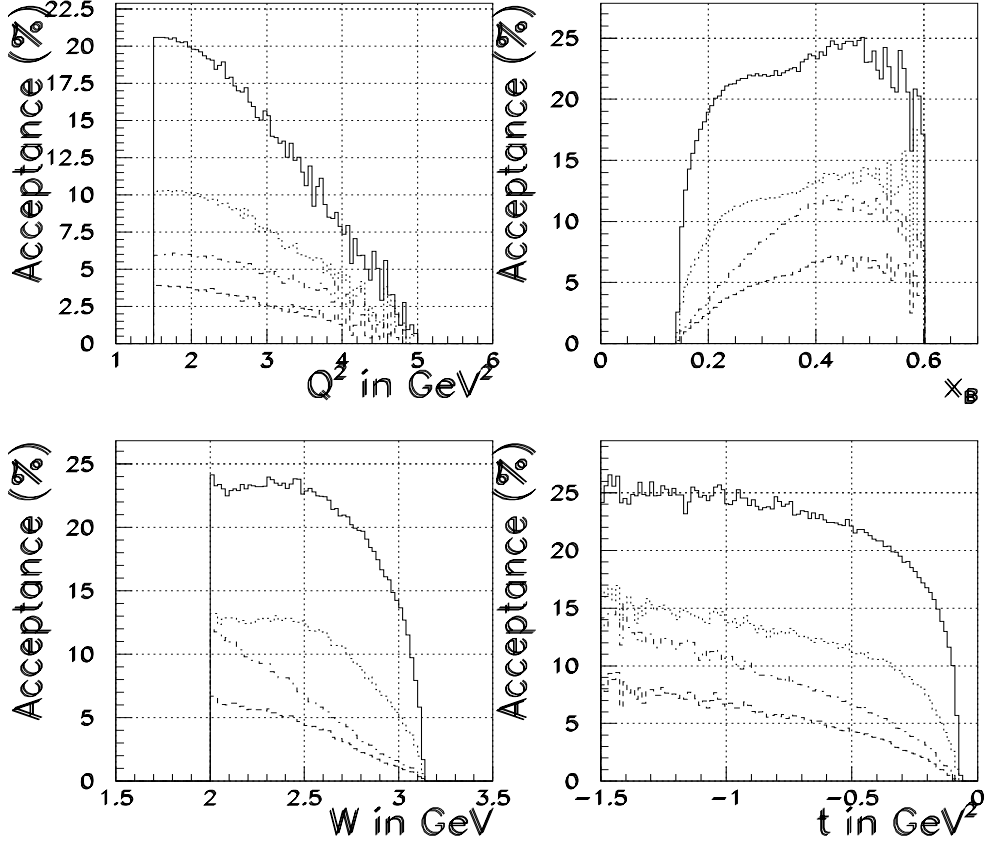- As Q^2 increases, t_{min} increases.

FIG. 10. Acceptance studies ; for the 4 kinematical variables Q^2, x_B, W and t, the figure shows

the percentage of accepted events in CLAS according to the criteria :

Full line : the 3 particles e,p,π^+ in the acceptance,

Dotted line : the 3 particles e,p,π^- in the acceptance,

Dotted-dashed line : the 3 particles e,π^+,π^- in the acceptance,

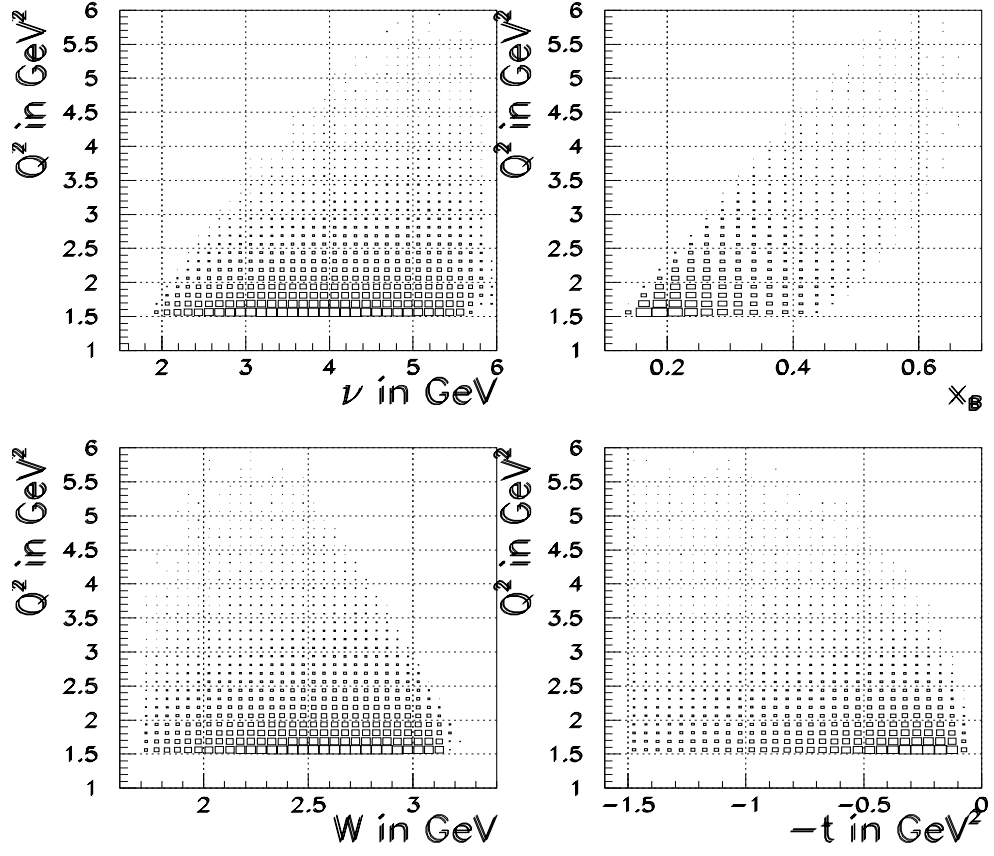Dashed line : the 4 particles e,p,π^+,π^- in the acceptance.

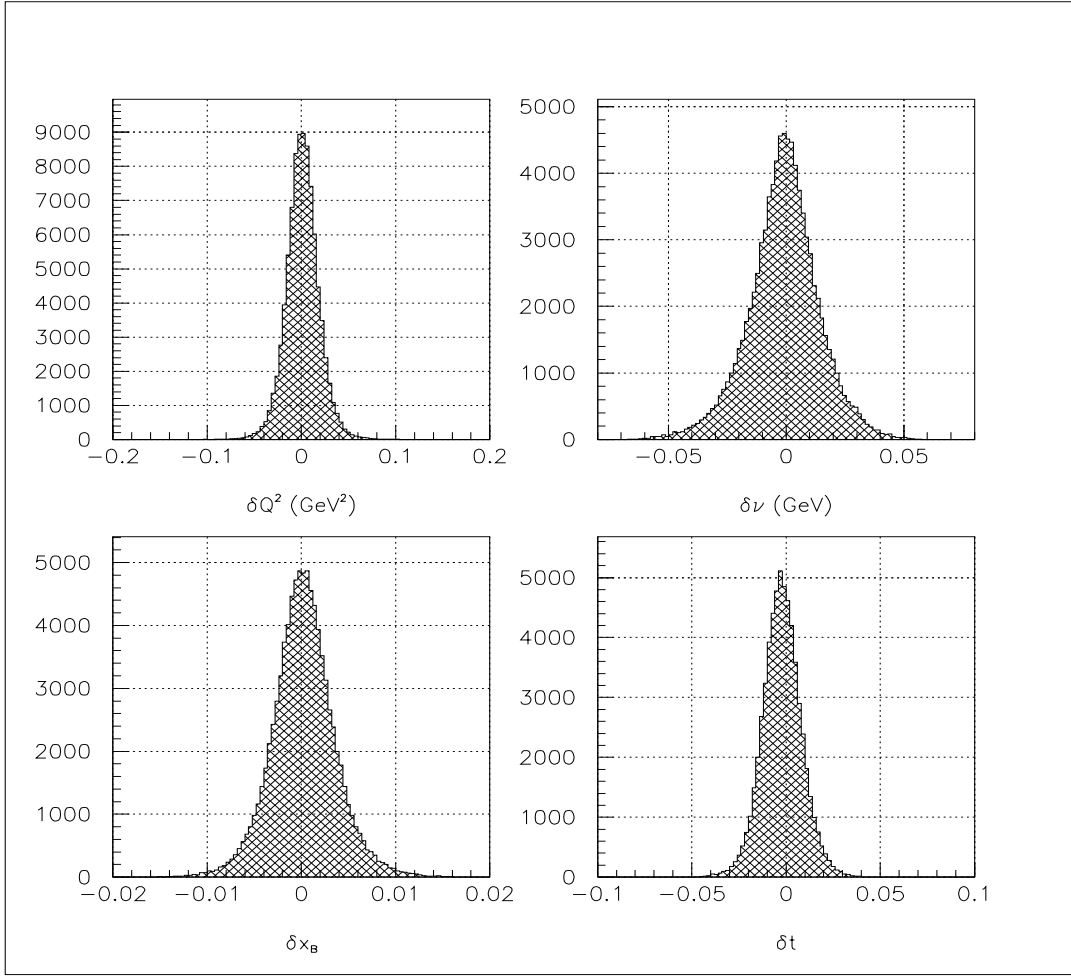FIG. 11. The correlations of Q^2 against x_B, W and t respectively.

FIG. 12. Resolutions obtained from FASTMC for the variables Q^2, ν, x_B and t.

2. Resolutions

Figure 12 shows the resolutions obtained from FASTMC for the variables Q^2, ν, x_B and t. For instance, the resolution on the scattered electron energy is of the order of ≈ 40 MeV (FWHM). It shows that one could, in principle, define "minimum" bins of the order $\Delta Q^2 \approx$ .2 GeV^2, $\Delta x_B \approx$ .01, $\Delta t \approx$ .05 GeV^2. In practice, in order to obtain reasonnable count rates, as shown in section IV F, we will take bins of the order $\Delta Q^2 = $ .2 GeV^2, $\Delta x_B = $ .1, $\Delta t = $ .1 GeV^2.

The expected very good resolution of the CLAS detector translates into a well recon-

21

structed ρ peak (see Fig. 13) by the missing mass method if one identifies and measures the kinematics of the scattered electron and of the proton $(e + p \rightarrow e' + p' + X)$:

$$E_X = E_e + M_p - E_{e'} - E_{p'}$$

$$p_{X(x)} = -p_{e'} \sin(\theta_{e'}) \cos(\phi_{e'}) - p_{p'} \sin(\theta_{p'}) \cos(\phi_{p'})$$

$$p_{X(y)} = -p_{e'} \sin(\theta_{e'}) \sin(\phi_{e'}) - p_{p'} \sin(\theta_{p'}) \sin(\phi_{p'})$$

$$p_{X(z)} = -p_{e'} \cos(\theta_{e'}) - p_{p'} \cos(\theta_{p'})$$

$$\rightarrow p_X = \sqrt{p_{X(x)}^2 - p_{X(y)}^2 - p_{X(z)}^2)}$$

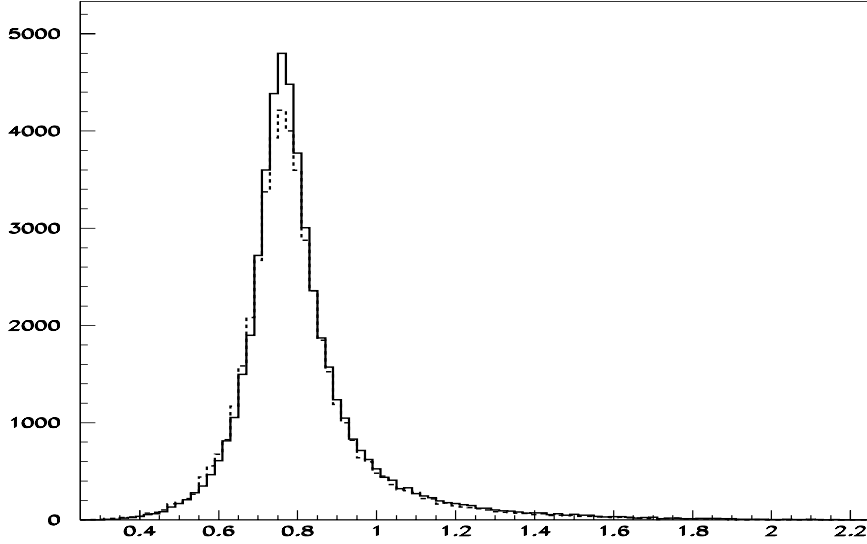$$\rightarrow M_X = \sqrt{E_X^2 - p_X^2} \tag{1}$$

FIG. 13. Reconstruction of the ρ peak by the missing mass technique, i.e. assuming the identification and the measure of the kinematics of the scattered electron and of the recoil proton. Full line : generated distribution (modified Lorentzian distribution with energy dependent width). Dotted line : reconstructed distribution (after FASTMC smearing). -The generated distribution has been renormalized to the reconstructed distribution to allow comparison between each other-.

We now turn to the decay angular distribution aspect. We recall that the angular distribution of the decay products of the ρ allows to access its polarization state. The detection of only one decay pion is enough to do so (if, of course, the scattered electron and proton are also detected) :

$$p_{cm} = \frac{\sqrt{(M_X^2 - 4m_\pi^2)}}{2}$$
$$E_{cm} = \sqrt{p_{cm}^2 + m_\pi^2}$$
$$\beta = \frac{p_X}{E_X}$$
$$\gamma = \frac{1}{\sqrt{1 - \beta^2}}$$
$$\hookrightarrow \cos(\theta_{cm}) = \frac{E_{\pi^+} - \gamma E_{cm}}{\gamma \beta p_{cm}} \tag{2}$$

Here, θ_{cm} is the polar angle of the π^+ relative to the direction opposite to the recoiling target in the ρ center of mass frame and p_{cm} and E_{cm} are respectively the momentum and the energy of the (π^+, π^-) system in the vector meson rest frame (see Fig. 15). Figure 16 shows the quality of reconstruction of $\cos(\theta_{cm})$ and the corresponding acceptance of the order of 20%. It can be seen however that the $\cos(\theta_{cm})$ acceptance is quite uniform but deviation will have to be taken into account when analyzing this angular distribution (acceptance correction). We will come back later on this decay angular issue in section IV E and see more precisely with a specific study how well one can extract the ρ polarization parameter $R = \frac{\sigma_L}{\sigma_T}$ from these $\cos(\theta_{cm})$ distributions.

We now proceed by the study of the Φ angle which is of interest for the study of SCHC as will be explained below (in section IV E). Figure 17 shows the quality of reconstruction of the Φ angle and the corresponding acceptance (of more 40%). This latter acceptance is more important because the detection of the proton alone suffices in principle to determine the orientation of the hadronic plane with respect to the leptonic plane (no pions are needed for this). However, it should be noted that the background will be more important if no

pion at all is detected besides the proton. This latter orientation defines the angle Φ (see figure 14).
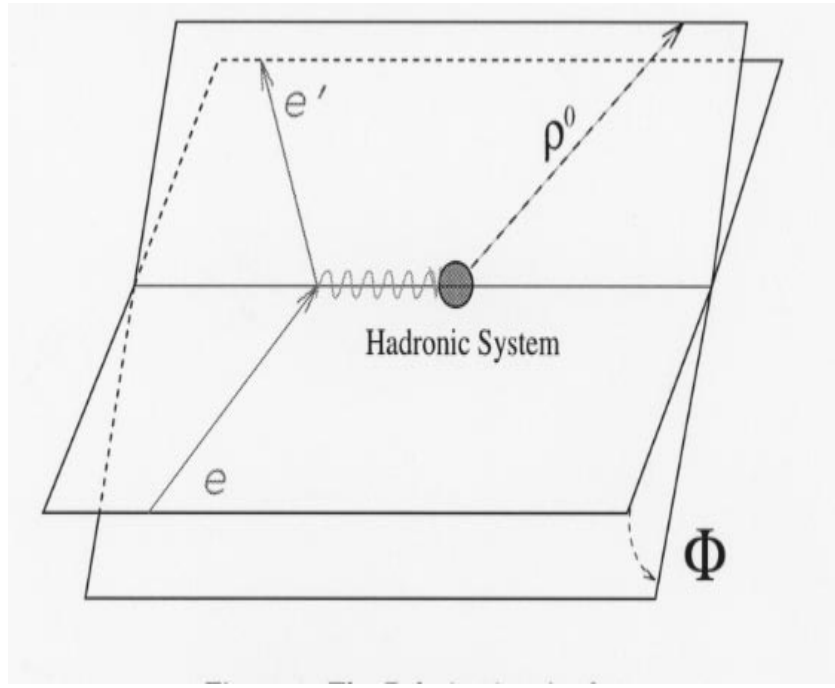
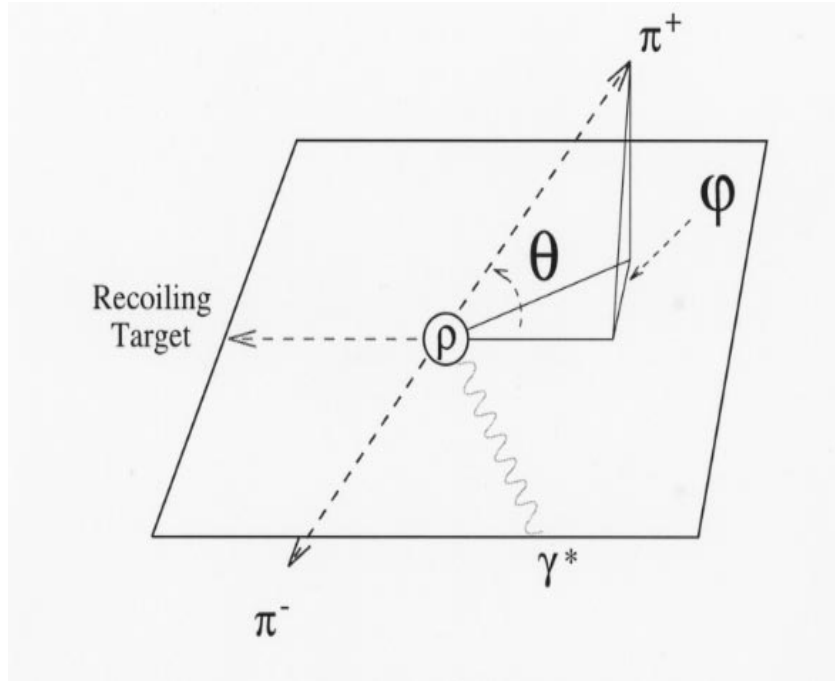FIG. 14. Definition of the angle Φ between the lepton and hadron planes.

FIG. 15. The polar angle θ_{cm} of the π^+ is defined, in the ρ rest frame, with respect to the z-axis antiparallel to the recoiling proton direction.
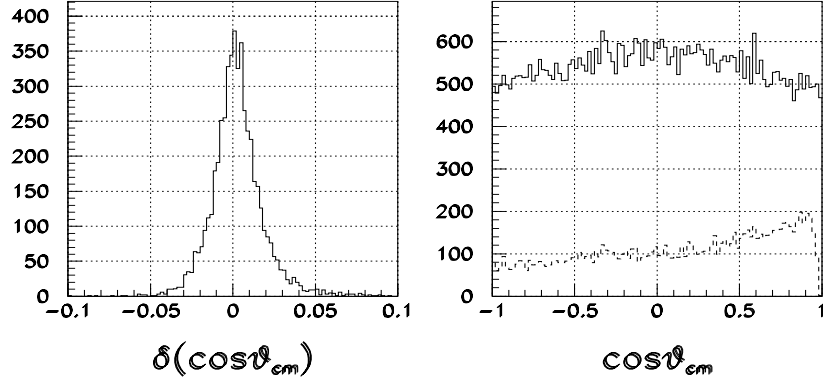
FIG. 16. Left plot : reconstruction resolution of the $\cos(\theta_{cm})$ variable (to analyze the ρ decay angular distribution). Bins of the order of $\Delta cos\theta_{cm} \approx .05$ can be defined in principle. Right plot : number of <u>accepted</u> e, p', π^+ events (dotted line) and number of <u>generated</u> events (full line).
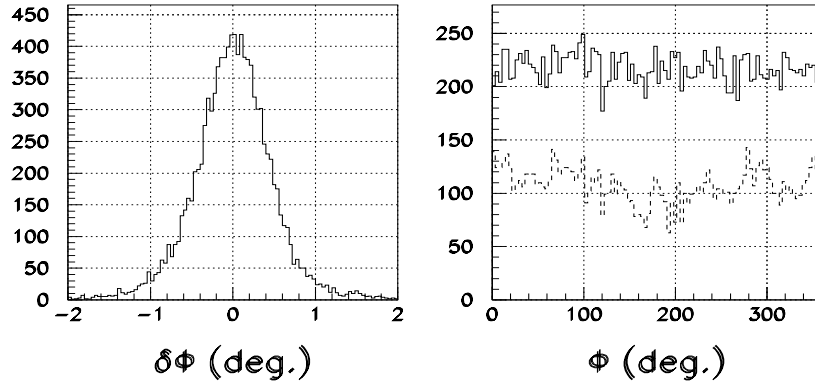

FIG. 17. Left plot : reconstruction resolution of the Φ angle (to test SCHC). Bins of the order of $\Delta\Phi \approx 2$ degrees can be defined in principle. Right plot : number of <u>accepted</u> e, p' events (dotted line) and number of <u>generated</u> events (full line)

26
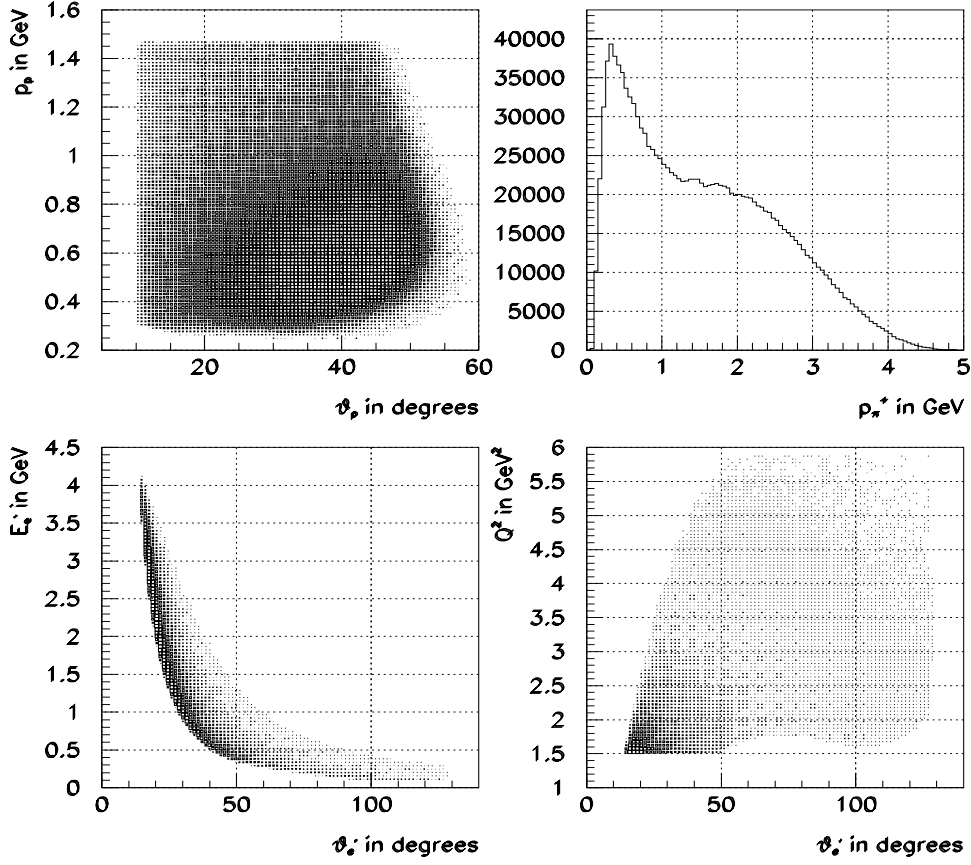
FIG. 18. a) (upper left plot) : Momentum of accepted protons vs proton angle (in lab).

b) (upper right plot) : Momentum distribution of accepted positive pions.

c) (lower left plot) : Scattered electron energy vs scattered electron angle (in lab) -for accepted

electrons-.

d) (lower right plot) : Q^2 against scattered electron angle (in lab) -for accepted electrons in CLAS

(By "accepted", it is meant in the CLAS acceptance but, of course, electrons scattered at larger

angles than 75° cannot contribute to the trigger and are thus considered lost)-.

Figure 18 shows the kinematical values (momentum, angles) of the protons, pions and

electrons in the kinematical domain of our concern (large Q^2, small t). It is seen in Fig.18a

that protons are produced at large laboratory angles and have a rather small momentum. The minimum momentum needed for a proton to be reconstructed is ≈ 300 MeV. Fig.18b shows the momentum distribution of the positive pions. It is seen that most of them ($\approx$ 70% GeV) have less than 2 GeV and should therefore be clearly identified by the time-of-flight technique. However, the remaining 30 % is not lost, but one will have then to take into account possible "contamination"/misidentification with kaons. The production rate of these latter is however expected to be much smaller compared to the pions. Fig.18c shows the correlation between the energy and the angle of the scattered electron. Some electrons have energies up to 4 GeV and some scatter up to very wide lab angles. Most of them are however scattered at angles less than 45° in the standard forward calorimeter. Finally, Fig.18d shows that large Q^2 (> 2.5 GeV^2) corresponds in general with large lab angles ($\theta_e >$ 20 ^{o}).

D. Background contributions

Estimation of background is of course difficult in these largely unexplored kinematical domains of large Q^2 ($Q^2 > 2$ GeV^2) and above the resonance region ($W > 2$ GeV). Two experiments have explored the "frontiers" of these regions. On the low Q^2 side (for 2<W<4 GeV), there are vector meson electroproduction data from DESY [18] and CORNELL [19]. In spite of their low statistics, the ρ peak came out in a rather clean way above a ≈ 10 % background (Fig. 7 for instance). It is seen that this background tends to increase as W decreases as one approaches the resonance region where competitive mechanisms (resonance formation for the most part) leading to the same final state (i.e. e', p, π^+, π^-) occur with relatively high cross sections. It would therefore be desirable to have some estimate of the $\pi^- \Delta^{++}$ contribution. Modelizations are currently under study [20] [21] to describe $\pi^- \Delta^{++}$ electroproduction above the resonance region, i.e. in the kinematical domain of the present experiment. At low Q^2, the reaction mechanism for $\pi^- \Delta^{++}$ production proceeds mainly through a contact interaction and a t-channel π-exchange process. These models will allow

28

us to estimate the residual $\pi^- \Delta^{++}$ electroproduction contribution under the ρ peak in the present experiment and have an idea of possible interference effects. These models can also be calibrated to some extent by several photo- and electroproduction experiments at lower energies (in the resonance region) that are currently taking place at CLAS. Also, correlation plots such as $M_{\pi^+\pi^-}$ vs $M_{p\pi\pm}$ (Dalitz plots) will allow to estimate and constrain such backgrounds modelizations.
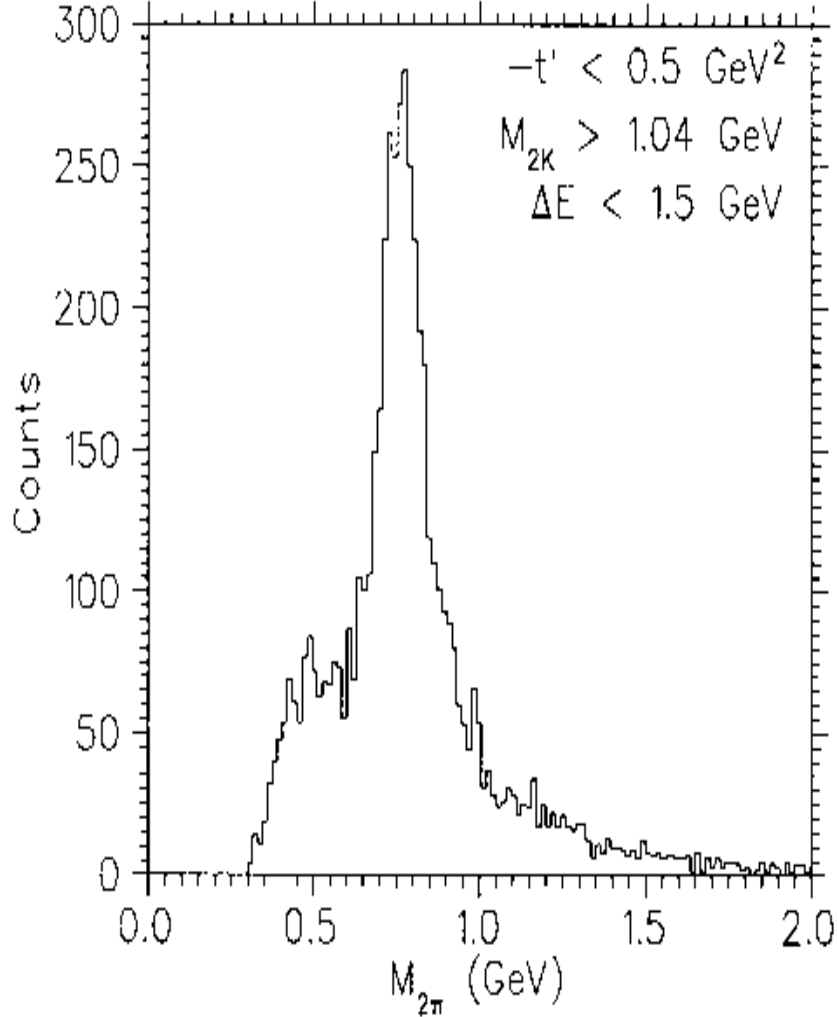

FIG. 19. Invariant mass spectrum of the "assumed" 2-pion system from a HERMES experiment (preliminary [17]) on a He^3 target (the HERMES experiment cannot -currently- distinguish between pions and kaons).

The HERMES experiment is also tackling the region of large Q^2 above the resonance

29

region. Figure 19 shows the ρ peak reconstruction at the kinematical regime $4 \lesssim W \lesssim 6$ GeV and Q^2 up to 5 GeV^2. Here also, the background under the peak appears to be ≈ 15 %.

E. Decay angular distribution analysis

1. $\cos \theta_{cm}$ distributions

As was stressed out in the previous section, one needs in this experiment to separate longitudinal from transverse ρ's. The technique is well known : the formalism linking the decay angular distribution to the polarization of vector mesons in electroproduction can be found for example in Ref. [25] (similar studies of the ρ decay angular distribution are part of other approved JLab proposals, see Ref. [26] [8]).

It is found that the $\cos(\theta_{cm})$ (see Fig. 15 for definition) distribution follows the form :

$$W\left(\cos(\theta_{cm})\right) = \frac{3}{4}\left\{1 - r_{00}^{04} + (3r_{00}^{04} - 1)\cos^2\theta_{cm}\right\} \tag{3}$$

(The angle θ_{cm} has been defined in section IV B). The matrix element r_{00}^{04} depends on Q^2 and W and is linked to the longitudinal polarization state of the ρ -for instance, $r_{00}^{04}=1$ (0) corresponds to pure longitudinal (transverse) polarization of the ρ respectively and, in terms of angular distribution, to $\frac{3}{2}\cos^2\theta_{cm}$ ($\frac{3}{4}\sin^2\theta_{cm}$) respectively-. Assuming s-channel helicity conservation (SCHC), one often links the ρ polarization to the virtual photon polarization and one defines :

$$R = \frac{\sigma_L}{\sigma_T} = \frac{1}{\epsilon}\frac{r_{00}^{04}}{1 - r_{00}^{04}} \tag{4}$$

The link is obvious : as r_{00}^{04} represents the longitudinal degree of polarization, $1 - r_{00}^{04}$ represents the transverse degree of polarization. One then divides by the degree of longitudinal polarization of the photons : ϵ. In the following, we will keep to this SCHC assumption. This premise can be checked in the data by measuring the longitudinal-transverse interference response function (R_{TL}) by making out-of-plane angle asymmetries for instance.

30

The quantity R has already been measured in many experiments. It is displayed as a function of Q^2 for instance (so, for a mixture of W values) in Figure 20. The increase of R with Q^2 is clear and means that longitudinal ρ's are dominant at large Q^2. However, in the $Q^2 \approx 3$ GeV^2 and $2 < W < 3$ GeV domain which concerns us, it is not known. We will therefore have to measure it in order to be able to select longitudinal ρ's.
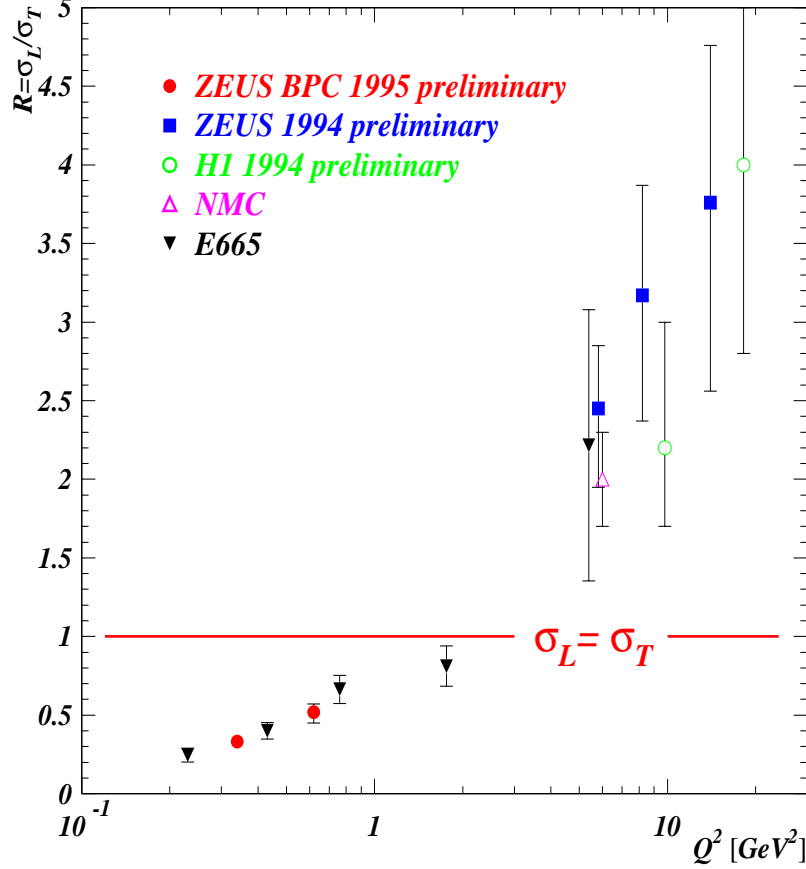
FIG. 20. World data of $R = \frac{\sigma_L}{\sigma_T}$ as a function of Q^2 (assuming SCHC) [15].

To estimate to which accuracy we will be able to measure R in our experiment, we generated events with the ratio R following the formula :

$$R = \xi^2 \frac{Q^2}{M_\rho^2} \tag{5}$$

This formula originating from a Vector Meson Dominance (VDM) approach [27] describes the data of Figure 20 at intermediate Q^2 (≈ 3 GeV^2) with the value $\underline{\xi^2 = .3}$.

31

Taking into account the acceptance and the resolution of FASTMC, we checked how well we could retrieve this ξ^2 value from simulated data. Figure 21 shows the number of events and distributions obtained for each (x_B, t) at different Q^2. The evolution with Q^2 from a $cos^2\theta_{cm}$ towards a $sin^2\theta_{cm}$ distribution shows that transverse ρ's dominate at large Q^2. At first sight, this result might appear surprising as the ratio $R = \frac{\sigma_L}{\sigma_T}$ increases with Q^2 (see fig. 20 and table I). However, from formula 4, it is clear that the relation between r_{00}^{04} and R implies ϵ which, at a 6 GeV beam energy, varies considerably : ϵ decreases from .77 at Q^2=1.6 GeV^2 to .14 at Q^2=1.6 GeV^2 for instance (see table I). Therefore, it means that, although R increases with large Q^2, longitudinal ρ's do not dominate at large Q^2 because they are suppressed by the ϵ factor at 6 GeV.

Quantitatively now, it can be seen, from fig. 20 and table I, that the results of the fit yielded respectively .291, .272 and .251 (to be compared with the original value .3) for the 3 successive Q^2 average values 1.6, 2 and 3 GeV^2 (see table I). Of course, the larger the Q^2 value, the less events in a given bin, the less accurate the fit. One can conclude from this study that one should be able to separate longitudinal from transverse ρ's at the 10-15% level (up to $Q^2 \approx 3$ GeV^2.
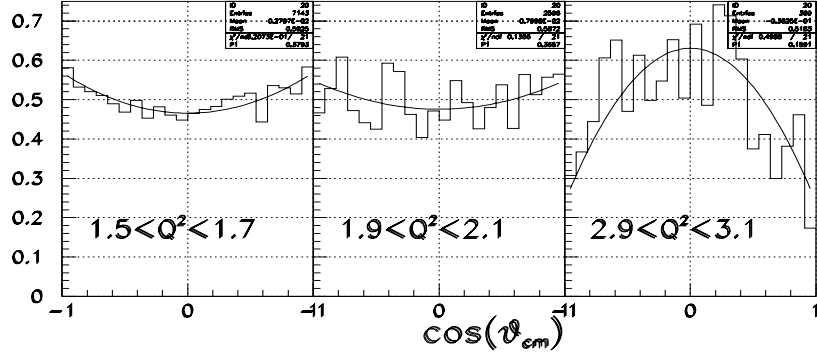
FIG. 21. Fits of the ρ decay pions angular distribution for 3 different values of Q^2 and for fixed x_B and t (.28< x_B < .32 and -.35< t <-.25). The curve shows the resulting fit by the function of equation 4 with r_{00}^{04} as the fitted parameter. Its value is displayed on the upper right corner of each plot (P1). One then easily retrieves the corresponding ξ^2 value through equations 4 and 5.

Q^2 (GeV^2)	"Generated" values				Fitted values	
	ϵ	ξ^2	R	r_{00}^{04}	r_{00}^{04}	ξ^2
1.6	.77	.3	.81	.37	.3793	.291
2	.63	.3	1.01	.39	.3657	.272
3	.14	.3	1.51	.18	.1591	.251

TABLE I. The table shows on the left part the <u>generated</u> values of R and r_{00}^{04} for ξ^2=.3 and for 3 different values of Q^2 (the value of ϵ at x_B=.3 is also indicated -to deduce the value of r_{00}^{04}-). The right part of the table shows the <u>fitted</u> values derived from the angular distributions weighted by the cross section and smeared by FASTMC. The fitted ξ^2 are in agreement at the 10-15% level with the "original" value of .3 depending on Q^2. Note that, although $R = \frac{\sigma_L}{\sigma_T}$ increases with Q^2, r_{00}^{04} decreases due to the values of ϵ which decrease with Q^2 -see Eq. 4-.

We now turn to the Φ (see Fig. 14 for definition) angular distribution which can be written in the most general form for an unpolarized beam according to :

$$\bar{\sigma}(\Phi) = 1 - \varepsilon \cos(2\Phi)\bar{R}_{TT} + \sqrt{2\varepsilon(1+\varepsilon)} \cos(\Phi)\bar{R}_{TL} , \qquad (6)$$

where the normalized response function $\bar{R}_{TT}$ and $\bar{R}_{TL}$ are given by

$$\bar{R}_{TT} = \frac{R_{TT}}{R_T + \varepsilon R_L} ,$$
$$\bar{R}_{TL} = \frac{R_{TL}}{R_T + \varepsilon R_L} .$$

If SCHC holds, the response functions R_{TT} and R_{TL} must be 0 and therefore the Φ angular distribution must be flat. This distribution is therefore a good test of SCHC. In order to estimate to which extent this observable is sensitive to any "violation" of SCHC, we generated events and reconstructed ("after"FASTMC) the Φ angular distributions for three cases : ($\bar{R}_{TT} = \bar{R}_{TL} = 0\%$), ($\bar{R}_{TT} = 0\%, \bar{R}_{TL} = 10\%$) and ($\bar{R}_{TT} = 10\%, \bar{R}_{TL} = 0\%$). The resulting Φ angular distributions and fits are displayed on figure 22. The numerical results are summarized in table II and show that one can retrieve the "input" values of $\bar{R}_{TT}$ and $\bar{R}_{TL}$ to less than 10% approximatively (in a given Q^2, x_B and t bin). One should notice that the ϵ factor ($\approx$.77 for this kinematics) in front of the $\bar{R}_{TT}$ term diminishes the weight of the $\cos(2\Phi)$ term and therefore $\bar{R}_{TT}$ is less accessible. A priori, the Φ angular distribution does not necessitate the detection of any pions (from the decay of the ρ) as the detection of the proton is enough to define the hadronic plane with respect to the leptonic plane (Φ is the angle between these two planes, see figure 14). The acceptance is roughly 2.5 times more important for a final state e', p' with respect to a final state e', p', π^+, and a priori the statistics should be increased for this kind of analysis. However, it has to be taken into account that the background will be more important if no pion at all is detected besides the proton.

We can conclude from this short study on the Φ angular distribution that one should be able to test SCHC to less than $\approx 10\%$. If we find that deviations from a flat Φ distribution

34

are indeed less than $\approx 10\%$, it means that helicity flip contributions such as $\gamma_T^* p \to p\rho_L$ are certainly negligible. In other words, this means that (to the $\approx 10\%$ level) longitudinal ρ's are mainly produced by longitudinal photons. Identifying longitudinal ρ suffices then to select the $\gamma_L^* p \to p\rho_L$ channel of interest.

On the other hand, deviations greater than $\approx 10\%$ (in a given kinematical range) would indicate that a substantial number of longitudinal ρ can come from transverse photons. In order to identify the channel of interest $\gamma_L^* p \to p\rho_L$, one would then have to really select longitudinal photons and this could only be done through a Rosenbluth separation. It is therefore important to quantify the degree of violation of SCHC (through the Φ angular distribution) if one wants to access the OFPD physics as exposed above.

"Generated" values		Fitted values	
$\bar{R}_{TT}$	$\bar{R}_{TL}$	$\bar{R}_{TT}$	$\bar{R}_{TL}$
0	0	-.042	.0005
0	.10	-.041	.101
.10	0	.06	-.0002

TABLE II. The table shows on the left part the generated values of $\bar{R}_{TT}$ and $\bar{R}_{TL}$ for 3 different combinations of values of Q^2. The right part of the table shows the fitted values derived from the Φ distributions weighted by the cross section and smeared by FASTMC.
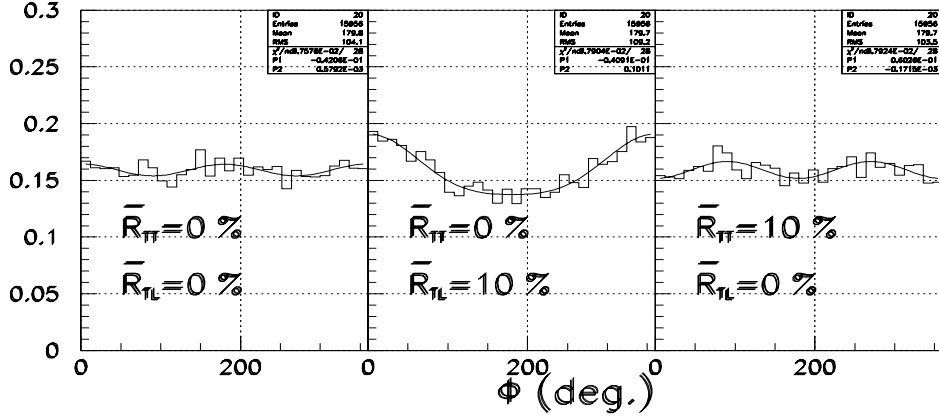
FIG. 22. Fits of the azimuthal angular dependence of the normalized (unpolarized) cross section $\bar{\sigma}(\Phi)$ according to Eq.(6) for different values of the response functions $\bar{R}_{TL}$ and $\bar{R}_{TT}$. The resulting fit values of $\bar{R}_{TT}$ and $\bar{R}_{TL}$ are displayed in the upper right corner of each plot (respectively $P1$ and $P2$). This was done for the following bins : $1.5 < Q^2 < 1.7$ GeV^2, $.28 < x_B < .32$ and $-.35 < t < -.25$ GeV^2.

F. Count rate estimates

Fig. 23 shows the number of counts expected for 400 h of beam time for the 5-fold differential cross section $\frac{d\sigma}{dk^e_{Lab} d\Omega^e_{Lab} dt}$ as a function of t at $x_B = .3$ (x_B value around which the OFPD contribution should be maximal) for different Q^2 ranges. It was assumed a luminosity of 10^{34} cm^{-2} s-1. The acceptances (of the order of 15-20% as was seen in the previous sections) and resolutions have been taken into account in this plot. It is seen that at Q^2 around 2 GeV^2 (and in relatively small t bins), the number of counts can amount to ≈ 1000 and to ≈ 100 around 3 GeV^2.

Fig. 24 shows an estimate of the accuracy with which we should be able to measure the observable $\frac{d\sigma_L}{dt}$ at fixed value of t as a function of Q^2, with the same beam time and luminosity. This observable is used to test the scaling behavior of the reaction mechanism as

36

a function of Q^2. The range reachable at JLab goes up to $Q^2 \approx 3.5$ GeV^2 for $x_B=.3$ which corresponds to a variation over approximatively a decade of the differential cross section. The error bars in this figure are statistical and include the effect of the resolution (given by FASTMC) of the kinematical variables needed to reconstruct this observable. However, it does not include any background contamination nor the estimated 10-15% error in separating longitudinal from transverse ρ's (see section IV E). Nevertheless, it should be clear that we should be able to extract the slope of this observable and to test if and at what value of Q^2 this $\frac{1}{Q^6}$ scaling behavior sets in.
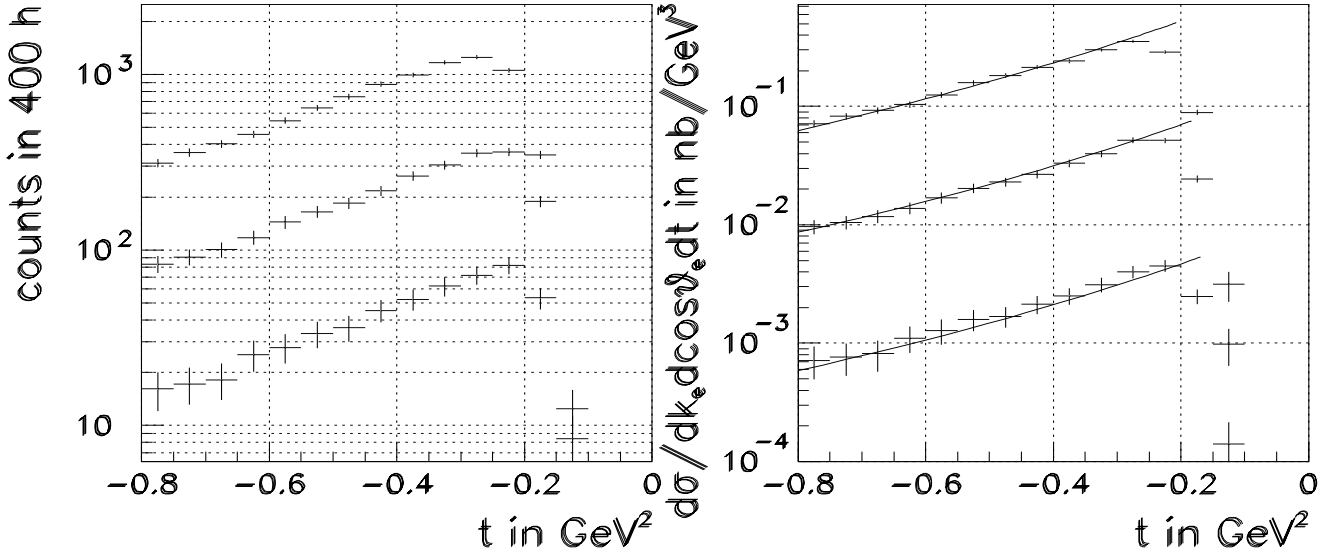
FIG. 23. Left plot : number of counts expected for 400 h of beam time on $\frac{d\sigma}{dk_{Lab}^e d\Omega_{Lab}^e dt}$ at $x_B=.3$ for different Q^2 values. Upper points/curve : 1.9$< Q^2 <$ 2.1 GeV^2; "middle" points/curve : 2.4$< Q^2 <$ 2.6 GeV^2; lower points/curve : 2.9$< Q^2 <$ 3.1 GeV^2. For all curves, .28$< x_B <$.32 and Δ t=.05 GeV^2. Right plot : the corresponding normalized cross-section ; the curve is the theoretical model which served as input to the event generator. The discrepancy at small t is due to the broad ρ width which is not taken into account in the theoretical model.
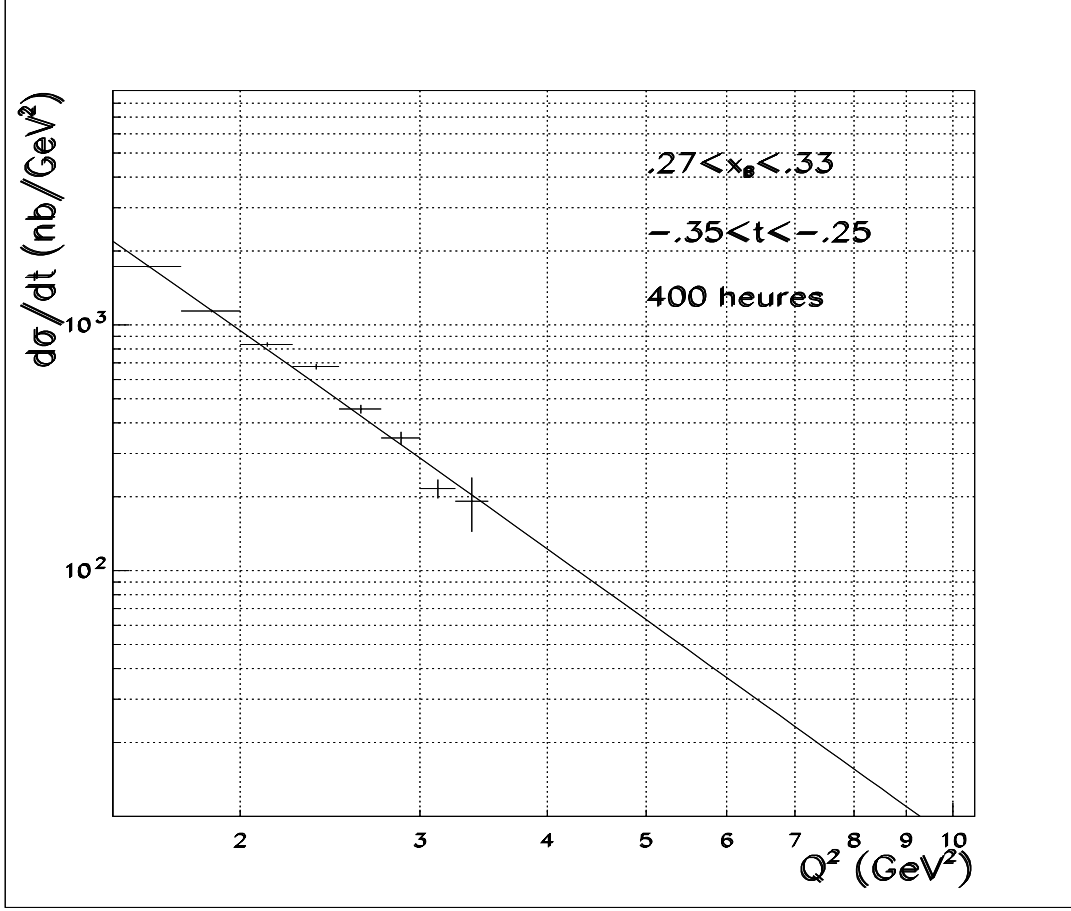
FIG. 24. Error estimate (statistical only) on the scaling behavior for the ρ_L^0 channel for $t = -.3$ GeV^2 and $x_B = .3$.

G. Trigger considerations

We propose to use an inclusive single electron trigger requiring energy deposition in the forward angle calorimeter and a signal in the Cerenkov counter in the corresponding sector. This was the trigger used during the $e1$ running period which was limited to a luminosity of 4×10^{33} cm^{-2}s^{-1}. During $e1$, the typical trigger rate was 550 Hz corresponding to a data transfer rate of 1.3 kB/s (70% live time). A top priority for Hall B is to increase the data acquisition rate to take data at the design luminosity of $\times 10^{34}$ cm^{-2}s^{-1}. The level 2 trigger

38

will be implemented this summer and will increase the electron selectivity of the trigger. At the same time, improvements are continuously being made to upgrade the DAQ system to take data at the design value of 1.5 kHz and 10 kB/s. These improvements will allow this experiment to acquire data at the proposed rate.

V. CONCLUSION

We have estimated in the previous section that the measurement of the ρ^0 electroproduction up to $Q^2 \approx 4$ GeV^2 and around $x_B = 0.3$ is feasible at JLab with the CLAS detector. Our program is first to measure the Q^2 dependence of the forward differential cross section to test if the Bjorken regime is reached. If so, the high expected count rates for the ρ^0_L channel, will open up a new virgin domain. This will eventually make it possible to perform for the first time an exploratory analysis of the (unpolarized) OFPD's.

To complete this measurement, we request the following running conditions :

- 400 hours of beam time. Note that the large amount of beam time is required by the count rate at high Q^2.

- LH_2 target

- $\mathcal{L} = 10^{34}$ cm^{-2} s^{-1}

- Full field, negative particles bend toward the axis

- Electron beam : $E_e = 6$ GeV or higher.

- Standard single electron trigger.

APPENDIX A: THEORETICAL FORMALISM OF THE OFPD'S

In this appendix we present more details of the theoretical formalism of the OFPD's. In the handbag diagrams for DVCS shown before (Fig.1), the lower blob represents the structure of the nucleon and it can be parametrized, at leading order PQCD in Q^2, in terms of 4 generalized structure functions $H, E, \tilde{H}, \tilde{E}$ which depend on 3 kinematical variables x, ξ and t to be defined shortly. More precisely, the light-cone matrix element associated with the "lower" blob of Fig. 1 is given by [*] :

$$\frac{1}{4} \left\{ (\gamma^-)_{\alpha\beta} \left[H^q(x,\xi,t) \, \bar{N}(p')\gamma^+ N(p) \ + \ E^q(x,\xi,t) \, \bar{N}(p')i\sigma^{+\kappa}\frac{\Delta_\kappa}{2m_N}N(p) \right] \right.$$
$$\left. +(\gamma_5\gamma^-)_{\alpha\beta} \left[\tilde{H}^q(x,\xi,t) \, \bar{N}(p')\gamma^+\gamma_5 N(p) \ + \ \tilde{E}^q(x,\xi,t) \, \bar{N}(p')\gamma_5\frac{\Delta^+}{2m_N}N(p) \right] \right\} , \quad (A1)$$

where N is the nucleon spinor and α, β are Dirac indices of the quark fields. In Eq. (A1), the OFPD's $H^q, E^q, \tilde{H}^q, \tilde{E}^q$ are defined for one quark flavor ($q = u, d$ and s). The quark light-cone momentum fraction x is defined by $k^+ = xP^+$ with $P = 1/2(p + p')$. The longitudinal momentum fraction ξ is defined by $\Delta^+ = -2\xi \, P^+$, where $\Delta \equiv p' - p$ and $t = \Delta^2$. Note that $2\xi \to x_B/(1 - x_B/2)$ in the Bjorken limit. The support in x of the OFPD's is $[-1, 1]$ and a negative momentum fraction corresponds to the antiquark contribution.

———————

[*]In the following we use light-cone components of a four-vector which are defined as $a^{\pm} = 1/\sqrt{2}(a^0 + a^3)$.

Note that the OFPD's come by pairs, two functions (H and E) are associated with the *vector* current and two functions ($\tilde{H}$ and $\tilde{E}$) are associated with the *axial vector* current.

These OFPD's obey some fundamental relations and sum rules which were derived by Ji [1]. For instance, they reduce, in the forward direction ($\Delta = 0$), to the well-known parton distributions obtained from DIS :

$$H^q(x,0,0) = q(x) \; , \tag{A2}$$

$$\tilde{H}^q(x,0,0) = \Delta q(x) \; , \tag{A3}$$

where $q(x)$ and $\Delta q(x)$ are the standard unpolarized and polarized quark distributions ($2f_1(x) = \sum_q e_q^2 q(x)$ and $2g_1(x) = \sum_q e_q^2 \Delta q(x)$).

The link between DIS and DVCS is obvious. The OFPD's are in fact an extension to the *exclusive* case of the standard parton distributions measured in *inclusive* deep inelastic lepton scattering (DIS). The analogy is best seen by considering the diagram of Fig. 25 which illustrates the relation between DIS and the forward matrix element of DVCS. With DIS, one has access only to the left part of the diagram (because only the scattered electron is detected) and therefore only to the forward matrix element of DVCS (with *both* photons of virtuality Q^2). Consequently, one measures an x dependence of the nucleon structure (through $F_{1,2}(x), g_{1,2}(x), ...$). In the DVCS reaction, the initial photon has virtuality Q^2 and one measures also the final photon which is now real and which is emitted at a small angle with respect to the virtual photon. This introduces an extra t and ξ dependence and in this way gives rise to nucleon structure functions which depend upon three variables ($H, E(x, \xi, t), \tilde{H}, \tilde{E}(x, \xi, t)$).
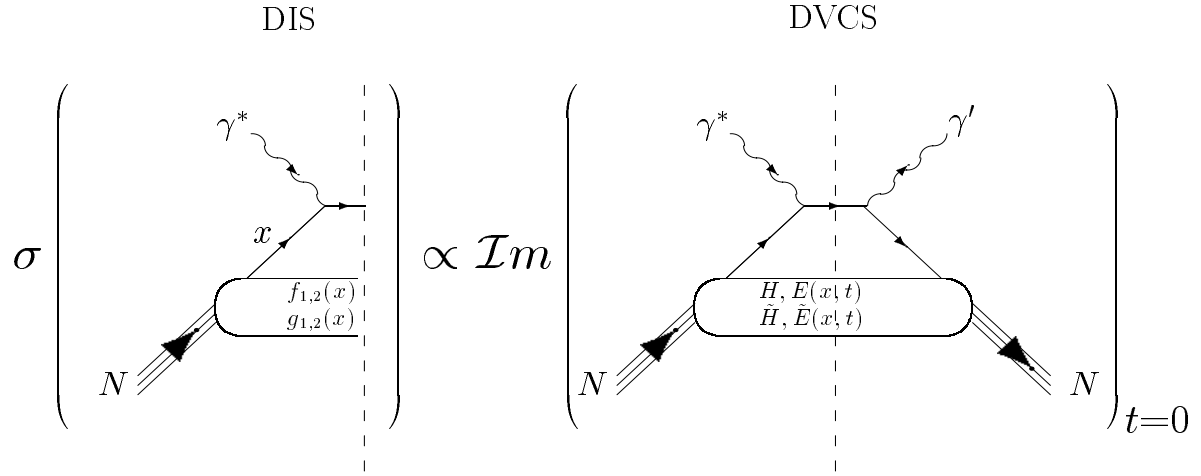
FIG. 25. The relation between DIS and the forward matrix element of DVCS. The optical theorem states that $\sigma_{DIS} \propto \mathcal{M}_{DIS}\mathcal{M}^*_{DIS} \propto \mathcal{I}m(\mathcal{M}_{DVCS}(\theta = 0))$.

The first moments of these OFPD's are related to the elastic form factors for one quark flavor as follows :

$$\int_{-1}^{+1} dx H^q(x,\xi,t) = F_1^q(t) , \quad \int_{-1}^{+1} dx \tilde{H}^q(x,\xi,t) = g_A^q(t) . \tag{A4}$$

$$\int_{-1}^{+1} dx E^q(x,\xi,t) = F_2^q(t) , \quad \int_{-1}^{+1} dx \tilde{E}^q(x,\xi,t) = h_A^q(t) . \tag{A5}$$

where F_1^q, F_2^q are the Dirac and Pauli form factors respectively, g_A^q is the axial form factor and h_A^q is the induced pseudoscalar form factor. Note that in the sum rules of Eq.(A5) the ξ-dependence drops out.

Finally, the second moment of the OFPD's gives the total quark contribution (sum of the intrinsic and orbital contributions) to the nucleon spin :

$$\frac{1}{2} \cdot \int_{-1}^{+1} dx \, x \, (H^q(x,\xi,t = 0) + E^q(x,\xi,t = 0)) = J_q \tag{A6}$$

where $\frac{1}{2} = J_q + J_g$ (quark and gluon contributions respectively) and $J_q = \frac{1}{2}\Delta\Sigma + L_q$ (intrinsic and orbital angular momentum respectively). Because the quark intrinsic spin contribution $\Delta\Sigma$ is measured through polarized DIS experiments (SMC, SLAC, HERMES), the mea-

surement of the OFPD's will allow to determine the quark orbital angular momentum to the nucleon spin.

[1] X. Ji, Phys.Rev.Lett. **78** (1997) 610; Phys.Rev.D **55** (1997) 7114.

[2] A.V. Radyushkin, Phys.Lett.B **380** (1996) 417; Phys.Rev.D **56** (1997) 5524.

[3] J.C. Collins, L. Frankfurt and M. Strikman, Phys.Rev.D **56** (1997) 2982.

[4] T. H. Bauer, R. D. Spital, D. R. Yennie and F. M. Pipkin, Rev.Mod.Phys. **50** (1978) 261.

[5] M. Vanderhaeghen, P.A.M. Guichon, M. Guidal, Phys.Rev.Lett. **80** (1998) 5064.

[6] P.A.M. Guichon and M. Vanderhaeghen, Prog.Part.Nucl.Phys., Vol.41 (1998), in press.

[7] Cebaf experiment E93-031, spokespersons M. Anghinolfi, J.M. Laget and C. Marchand.

[8] Cebaf experiment E93-022, spokespersons H. Funsten, P. Rubin and E. Smith.

[9] M. Arneodo et al., Nucl.Phys. **B429** (1994) 503.

[10] M.R. Adams et al., Z.Phys.C **74** (1997) 237.

[11] M. Derrick et al., Phys.Lett.B **356** (1995) 601.

[12] S.J. Brodsky et al., Phys.Rev.D **50** (1994) 3134.

[13] L. Frankfurt, W. Koepf and M. Strikman, Phys.Rev.D **54** (1996) 3194.

[14] H.L. Lai et al., Phys.Rev.D **51** (1995) 4763.

[15] J.A. Crittenden (for ZEUS Collaboration), presented at Photon'97, May 1997.

[16] U. Stiegler, Phys.Rep. **277** (1996) 1.

[17] J.E. Belz and G. Van der Steenhoven, private communication.

[18] P. Joos et al., Nucl.Phys. **B113** (1976) 53.

[19] D.G.Cassel et al., Phys.Rev.D **24** (1981) 2787.

[20] L. Murhpy and J.M. Laget, work in progress.

[21] H. Holvoet and M. Vanderhaeghen, work in progress.

[22] M. Morlet and J. Van de Wiele, private communication.

[23] E. S. Smith, "Fast Monte Carlo Program for the CLAS Detector", CLAS-Note 90-003, Feb 1990.

[24] M. Guidal, "GEANT simulation of the CEBAF Large Acceptance Spectrometer", Master's Thesis, University of South Carolina, 1993.

[25] K. Schilling and G. Wolf, Nucl. Phys. **B61** (1973) 381.

[26] Cebaf experiment E94-109, spokesperson P.L. Cole.

[27] J. J. Sakurai, Phys.Rev.Lett **22** (1969) 981.